



# Impact of Thermal Electrode Activation on Electrocatalyst Performance in KCrPDTA/K<sub>4</sub>Fe(CN)<sub>6</sub> Flow Batteries

Talia Echeverria,<sup>[a, b]</sup> Francesco Bernasconi,<sup>[a]</sup> Paweł P. Ziemiański,<sup>[a]</sup> and David Reber<sup>\*[a]</sup>

Improving electrode performance is crucial for increasing energy efficiency and power density in redox flow batteries. Here, we study the effects of thermal activation of carbon paper electrodes on the performance of bismuth as an electrocatalyst in high-voltage KCrPDTA/K<sub>4</sub>Fe(CN)<sub>6</sub> flow batteries. While thermal activation improves wettability and surface area, it also

leads to the formation of large, agglomerated bismuth deposits that reduce Coulombic efficiency. Although bismuth lowers cell resistance and enhances voltage efficiency, it promotes parasitic hydrogen evolution depending on its morphology, underscoring the need for optimized catalyst deposition techniques.

## Introduction

Global renewable capacity additions increased by 50% to nearly 510 GW in 2023, marking the fastest growth rate in two decades. This rapid expansion poses unprecedented challenges for power grids due to mismatches between supply and demand, creating a critical need for energy storage to shift power from when it is generated to when it is needed. Redox flow batteries (RFB) are promising for long-duration energy storage, enabling inter- to multi-day storage, which is crucial for continued integration of renewable power sources.<sup>[1]</sup> However, current systems are limited by high costs and low energy density, and major research efforts have thus focused on the development of highly soluble active species to increase energy density that are based on abundant raw materials. Yet, it has been shown that cell-level energy density is relatively unimportant regarding system level footprints and that the typical approach of using very concentrated electrolytes invokes many challenges related to viscosity and ionic strength of the electrolyte.<sup>[2]</sup> Power density, on the other hand, is much more economically important as the power components (the cell stacks) dominate overall cost and practical systems often require fast charge rates, for example, to buffer the few hours a day of excess solar production.<sup>[2a,3]</sup> Therefore, the key to further improve RFBs is to develop high-voltage batteries that use low-cost electrolytes and can operate at high current densities while maintaining good energy efficiency. This approach reduces stack size and enables efficient electrolyte utilization, reducing overall capital costs.<sup>[4]</sup>

Chelating transition metal cations is a promising approach for developing new RFB electrolyte materials that enable high

cell voltages. Chelation can significantly alter a metal ions' pH stability, redox potential, and solubility. For example, 1,3-propylenediaminetetraacetic acid (PDTA) chelation of Cr<sup>3+</sup> ions shifts the Cr<sup>3+</sup>/Cr<sup>2+</sup> reduction potential toward more negative values, significantly improves redox kinetics, and inhibits hydrogen evolution.<sup>[5]</sup> The solubility of the potassium salt KCrPDTA reaches up to 1.5 M, which is on par with vanadium based systems.<sup>[6]</sup> Flow batteries with KCrPDTA as negative electrolyte and ferrocyanide/ferricyanide as positive electrolyte operate at a cell voltage of 1.6 V, compared to 1.3 V for vanadium-based systems, and are one of only a few cell chemistries that achieve peak discharge power densities of  $> 1 \text{ W cm}^{-2}$ .<sup>[7]</sup> In contrast to typical vanadium- or iron-chromium RFBs that employ highly-acidic electrolytes, these cells operate at near-neutral pH (8.5), which is advantageous for large-scale industrial manufacturing and reduces the risk of hydrogen evolution. Notably, electrolyte tank costs, an overlooked factor in flow battery economics, are significantly lower for non-caustic media.<sup>[8]</sup>

While the KCrPDTA/K<sub>4</sub>Fe(CN)<sub>6</sub> system shows promise, enhancing its power density is critical to reducing costs and lowering the total area specific resistance (ASR) is essential to advance commercialization.<sup>[9]</sup> Electrochemical cells encounter activation, ohmic, and mass transfer overpotentials, contributing to charge transfer, ohmic, and mass transport resistances.<sup>[4b]</sup> The conductivity of the electrolyte and the ion exchange capacity of the membrane affect ohmic resistance, mass transfer is dominated by electrolyte viscosity and flow rate, and charge transfer is governed by the kinetics of the active species.<sup>[7,9–10]</sup> Therefore, electrode treatments such as thermal activation, chemical etching, coatings, or doping have been explored, improving the power performance of, particularly acidic vanadium-based, RFBs.<sup>[11]</sup> Thermal activation of carbon electrodes up to about 500 °C has become a standard practice for acidic RFBs as it increases surface area, improves wettability, and introduces functional groups that serve as active sites for redox reactions.<sup>[12]</sup>

The introduction of electrocatalysts is another common strategy to reduce ASR. A plethora of materials have been studied, with bismuth often being chosen for its non-toxic nature and low cost, making it industrially viable.<sup>[13]</sup> The

[a] T. Echeverria, F. Bernasconi, P. P. Ziemiański, D. Reber  
Empa, Swiss Federal Laboratories for Materials Science and Technology,  
8600 Dübendorf, Switzerland  
E-mail: david.reber@empa.ch

[b] T. Echeverria  
University of Picardie Jules Verne, 80000 Amiens, France  
Supporting information for this article is available on the WWW under  
<https://doi.org/10.1002/batt.202400696>

working mechanism is still contested in literature, with explanations ranging from reduced charge transfer resistance, increased surface area, to inhibition of the hydrogen evolution reaction (HER) in acidic media via formation of  $\text{BiH}_x$  species.<sup>[13a,c,14]</sup> However, such species are not readily formed at near-neutral or basic pH and little information is available on the performance of metallic electrocatalysts in these environments. Importantly, studies on the interplay between thermal electrode activation and deposition behavior of electrocatalysts in near-neutral pH systems are absent in literature.

Here, we explore methods to enhance the power performance of high-voltage  $\text{KCrPDTA}/\text{K}_4\text{Fe}(\text{CN})_6$  RFBs by investigating the effects of thermal activation of carbon electrodes on cell performance and electrocatalyst morphology. As expected, thermal activation enhances wettability and surface area of bare electrodes, but we find that it results in large, aggregated bismuth deposits that significantly reduce Coulombic efficiency (CE). While bismuth reliably improves voltage and energy efficiency (VE and EE), it also promotes parasitic hydrogen evolution, depending on its morphology, highlighting the need for optimized catalyst deposition techniques.

## Results and Discussion

### Electrode Characterization

Sigracet 39 AA carbon papers consist of polyacrylonitrile-based fibers and a flaky carbonized binder.<sup>[15]</sup> Bismuth plating on carbon paper electrodes was performed from a  $\text{Bi}^{3+}$ -containing solution using a two-step galvanostatic protocol to initiate nucleation, followed by a slow growth step. Scanning electron microscopy (SEM) images show particles decorating the electrode surface (Figure 1 and Figure S1), confirmed as bismuth via energy-dispersive X-ray spectroscopy (Figures S2–S4). Non-activated (NA) electrodes display bismuth particles ( $0.4\text{--}2\ \mu\text{m}$ ) primarily on the flaky binder, while samples treated at  $150^\circ\text{C}$  in air (150C) show slightly larger particles ( $0.4\text{--}3\ \mu\text{m}$ ). In stark contrast, electrodes treated at  $400^\circ\text{C}$  (400C) show much larger agglomerates ( $6\ \mu\text{m}$ ). The microstructure reflects the cell voltage observed during electrodeposition: NA and 150C samples show similar values of about 1.50 V and 1.45 V for the nucleation and growth steps, respectively, while the cell voltage

with 400C electrodes is 250 mV lower for both steps (Figure S5). Higher voltages represent a higher driving force, creating nuclei on any available sites through instantaneous nucleation, resulting in many small bismuth deposits. Meanwhile, the lower potential on 400C samples indicates more favorable surface conditions and easier, progressive nucleation with fewer but subsequently growing nuclei, leading to larger agglomerates.

The hydrophobicity of carbon papers hinders surface wetting, effectively reducing the active surface area available to the electrolyte for electrochemical reactions. Wetting measurements showed poor wetting for NA and 150C electrodes, with contact angles of  $143 \pm 2^\circ$  and  $124 \pm 3^\circ$ , respectively (Figure S6 and Table S1). In contrast, the thermal treatment at  $400^\circ\text{C}$  significantly improved wettability, reducing the contact angle to  $22 \pm 4^\circ$ . This improvement is attributed to the introduction of oxygen functional groups from surface oxidation.<sup>[4a,12a,d]</sup> To investigate the effect of thermal treatments on our carbon-based electrodes, we characterized vibration modes of pristine and heat-treated electrodes via Raman spectroscopy. Perfect graphite crystals show only one Raman band at  $1575\ \text{cm}^{-1}$ , commonly called the G peak,<sup>[16]</sup> which is assigned to the vibration of  $\text{sp}^2$  bonds of in-plane carbons, while non-perfect graphitic materials also show the presence of the D peak at approximately  $1355\ \text{cm}^{-1}$ , which is attributed to the breathing mode of the rings.<sup>[17]</sup> The ratio between the D/G peaks has been extensively used to characterize the degree of disorder in carbon materials or a measure of the defects on the surface of the carbon papers.<sup>[12d]</sup> Raman mapping of electrode samples shows characteristic bands with different relative intensities for the fibers and flakes with the higher D/G ratio of the fibers indicating a more defective structure (Figure 2 and Table S2).<sup>[18]</sup> Increasing the treatment temperature leads to higher D/G ratios on both flakes and fibers, confirming an increase in disorder in the graphitic materials through thermal activation. Notably, this was previously observed only in spot-measurements, and the mapping data confirms the global effect of activation on the carbon paper.<sup>[4a]</sup>

The specific surface area (SSA) of carbon papers was determined using BET theory with nitrogen and krypton gases (Figure S7, Table S3). For samples with low surface areas ( $\sim 1\ \text{m}^2\ \text{g}^{-1}$ ) the results using nitrogen yielded errors  $>100\%$  and are not presented. Adsorption measurements show a dramatic increase in SSA from  $1.1\text{--}1.2\ \text{m}^2\ \text{g}^{-1}$  for NA and 150C

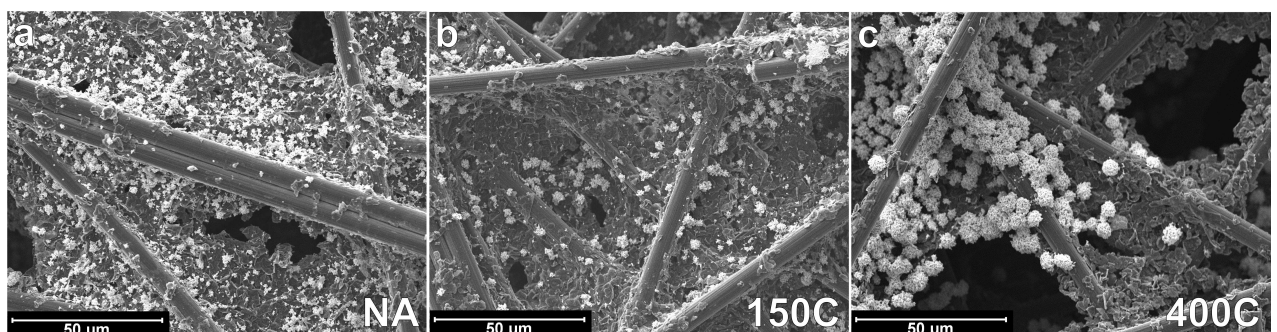
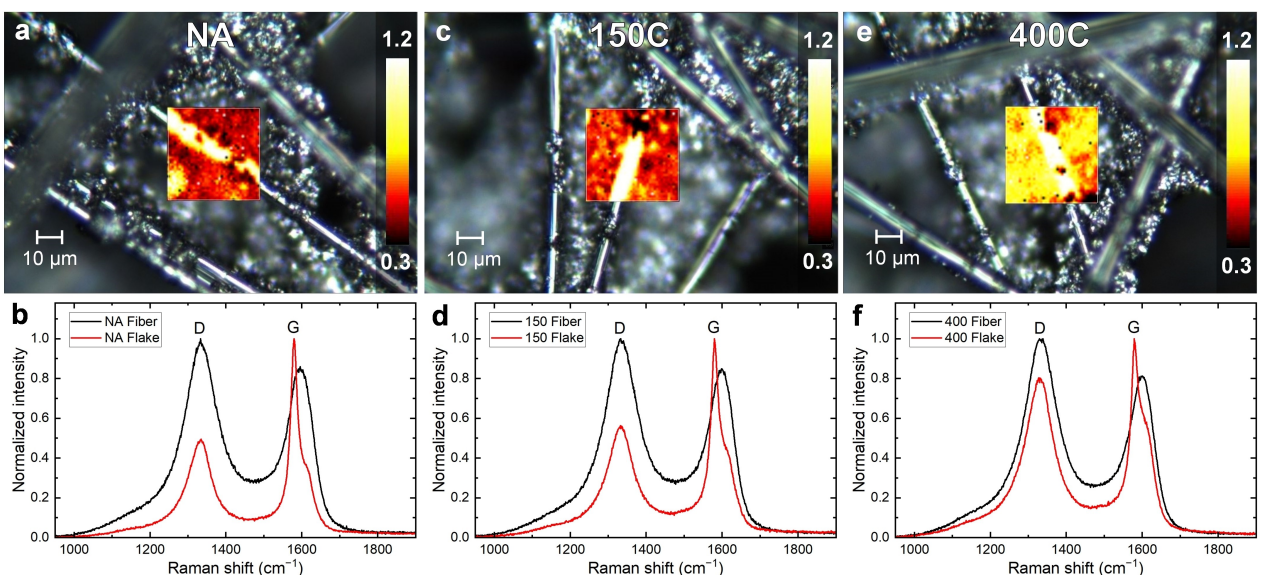


Figure 1. SEM images of bismuth-decorated carbon electrodes. Samples are a) non-activated, b) activated at  $150^\circ\text{C}$ , and c) activated at  $400^\circ\text{C}$ .



**Figure 2.** Micrographs of carbon papers with Raman mapping overlays displaying the D/G peak ratio and representative spectra of fibers and flakes for a,b) NA electrodes, c,d) 150C electrodes, and e,f) 400C electrodes.

samples to  $168 \text{ m}^2 \text{ g}^{-1}$  for 400C electrodes, consistent with the literature.<sup>[4a]</sup> Most of the SSA increase is related to the generation of micropores ( $< 2 \text{ nm}$ ), invisible in SEM (see Table S3). Interestingly, the addition of bismuth particles on the surface of NA electrodes increases the SSA by about 20%, while for 400C electrodes, a marked decrease is observed. This suggests that the bismuth deposits have a relatively low specific surface area, comparable to pristine carbon paper, and that for electrodes activated at  $400^\circ\text{C}$ , high-surface, microporous carbon is blocked by large bismuth deposits. Micropores may also be clogged in another way, as mass dilution of the high-surface 400C electrode with low-surface Bi particles ( $< 10 \text{ wt.\%}$ ) cannot fully explain the SSA drop by  $\sim 50\%$ .

Since the SSA determined by BET does not necessarily correspond to the electrochemical active area, we further characterized the electrodes via electrochemical double layer capacitance measurements (Table S3, Figure S8). Corroborating the BET results, the double layer capacitance increases significantly after thermal activation, indicating a large increase in the electrochemically active surface area.<sup>[12a]</sup> The bismuth particles slightly increase the double layer capacitance for the NA and 150C samples, but have little effect on the 400C electrodes.

Overall, the 400C electrodes show enhanced hydrophilicity, greater structural disorder, and a significant increase in surface area, suggesting improved performance in flow batteries.<sup>[12d,18]</sup> Conversely, larger bismuth agglomerates are expected to be less effective in improving redox kinetics than fine, homogeneously distributed particles. Notably, the constant-current protocol does not allow for differentiation of the impact of overpotentials and surface energy on the nucleation rates. Therefore, constant-potential electrodeposition would be better suited to account for variations in overpotential during the deposition process.

### Impact on Peak Discharge Power Density and Rate Capability

To evaluate the impact of electrode treatment and bismuth functionalization on the overall performance of KCrPDTA/K<sub>4</sub>Fe(CN)<sub>6</sub> flow batteries, we first focus on peak discharge power density and rate capability. These metrics are crucial for determining how electrode modifications affect power output and efficiency at different states of charge (SOC) and cycling rates. Before each experiment, the ASR of the cells was measured using linear voltage sweeps (Table S4, Figure S9). After ASR measurements, the  $5.3 \text{ cm}^2$  cells were cycled five times to 80% SOC at 500 mA with voltage cut-offs of 2.1 and 0.7 V to establish a baseline, followed by peak discharge power tests. Charging was performed at a constant current of 500 mA to 20, 40, 50, 60, 80, and 90% SOC, and discharging was performed using a controlled voltage sweep of  $200 \text{ mV s}^{-1}$  (Figure S10).

Bismuth functionalization significantly enhances the maximum power density across all electrode treatments, with improvements ranging from 13% to 24% (Figure 3a, Table S5). This increase is primarily attributed to the reduction in ASR. More specifically, impedance measurements at 50% SOC show the disappearance of a feature at 4–8 kHz with bismuth, attributed to charge transfer resistance (Table S3), while the process assigned to mass transfer (1–4 Hz) remains unaffected (Figure S11). The 400C-Bi electrodes showed the highest peak discharge power density, reaching  $1.33 \text{ W cm}^{-2}$  at a current density of  $1.52 \text{ A cm}^{-2}$  at 90% SOC. These results far exceed previous peak discharge power densities of  $0.62 \text{ W cm}^{-2}$  reported for the same cell chemistry and membrane at room temperature.<sup>[7]</sup> Interestingly, despite the 400C electrodes having a higher surface area, the NA-Bi electrodes enabled comparable peak discharge power density. This highlights the dominant role of bismuth in improving performance, independent of

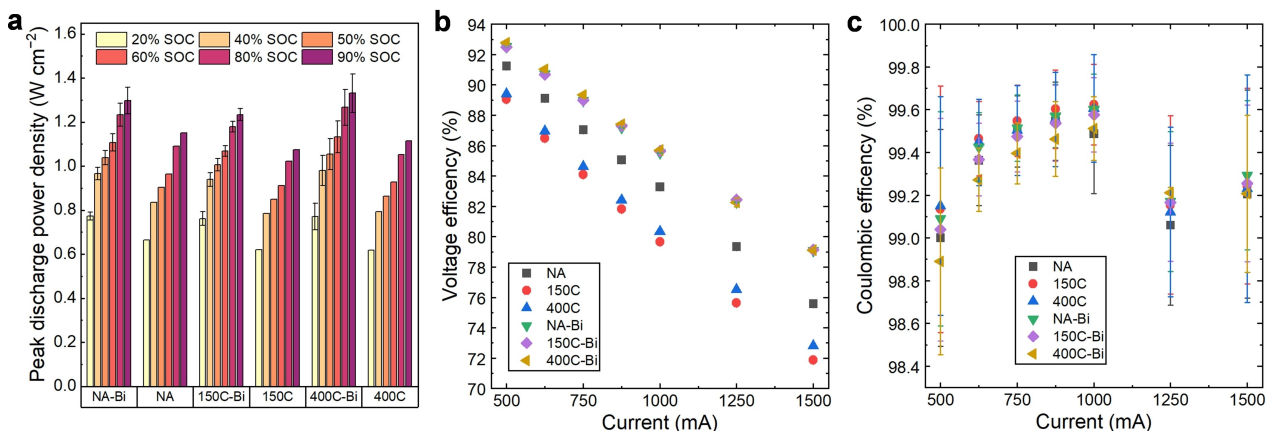


**Figure 3.** Comparison of peak discharge power density and rate capability. a) Peak discharge power density at various states-of-charge with all types of electrodes, b) voltage efficiency and c) Coulombic efficiency versus cycling current.

wettability or surface area, at least related to pores narrower than 2 nm. The OCV at each SOC remained unaffected by electrode treatments (Figure S12).

To further investigate the impact of electrode modifications on rate capability, the cells were cycled five times to 80% SOC at increasing currents, ranging from 500 to 1500 mA. At each current, the cells reached their target capacities corresponding to 80% SOC (Figure S13). The average VE and CE show a clear improvement of VE on bismuth functionalized electrodes at all cycling rates, in agreement with lower ASR as discussed above (Figure 3b). Standard deviations of the average VE at a given current are less than 0.1%. The CE increases from 99.3% to 99.7% with increasing cycling rates, suggesting that higher currents mask the effects of undesirable side reactions, such as hydrogen evolution, by reducing the time available for these reactions to occur (Figure 3c).<sup>[19]</sup> At 1250 mA and 1500 mA, CE is decreased, indicating the onset of mass transfer limitations. Notably, the electrodes without bismuth exhibit higher CE at all currents, in contrast to the hypothesis that bismuth suppresses water reduction. Particularly the 400C-Bi cells show significantly decreased CE, suggesting that the morphology of bismuth deposits plays a critical role. An additional 10 cycles at 500 mA

were performed after the rate test showing that capacities recovered to values comparable to the initial cycles, highlighting the resilience of the cell chemistry to high current cycling.

### Impact on Coulombic Efficiency

While bismuth functionalization clearly improves peak discharge power density and rate capability, its impact on CE shows a different trend. Extended cycling experiments over 50 cycles at 500 mA were performed using a thicker membrane to further highlight the differences in CE, as CE is a critical metric for long-term cycling stability. Although the thicker membrane increases ASR (Table S4), it helps prevent crossover, allowing inefficiencies to be attributed primarily to electrochemical processes at the electrodes. The average CE, VE, and EE values across the 50 cycles are shown in Figure 4. For clarity, error bars are omitted from the graph and are only shown in Figure S14.

In contrast to the improvements in power density, bismuth functionalization negatively affects CE for the 400C-Bi electrodes. Electrodes without bismuth showed consistently high CE,

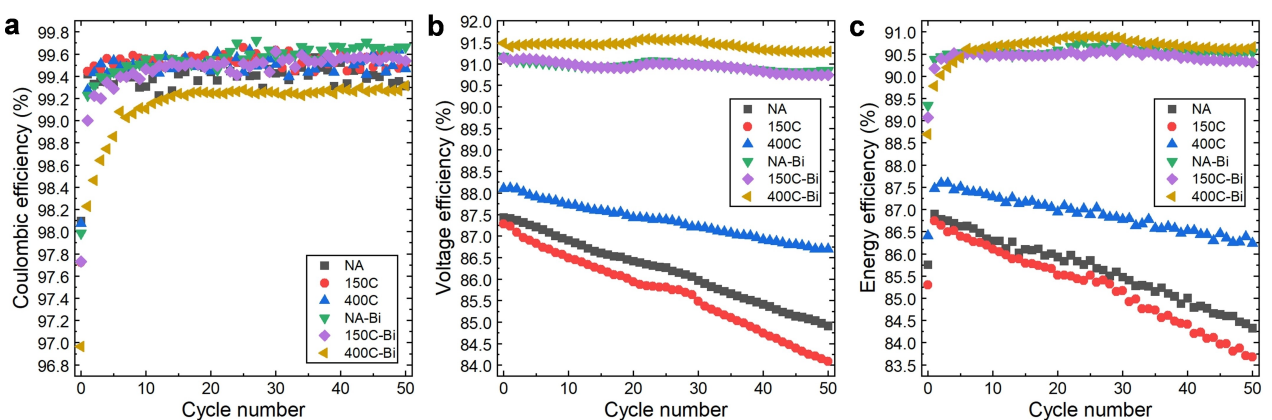


**Figure 4.** Extended cycling tests with all types of electrodes. a) Coulombic efficiency, b) voltage efficiency, and c) energy efficiency versus cycle number. Error bars are omitted for clarity and are shown in Figure S12.

averaging 99.4% for NA electrodes and 99.5% for thermally treated electrodes, and slightly improved and more stable VE. Adding bismuth led to marginal increases in CE for NA electrodes, while 150C electrodes showed slightly lower CE in the initial cycles. A significant drop of up to  $>1\%$  in CE was observed with the 400C-Bi electrodes. To assess the statistical significance of differences in Coulombic efficiency among the six electrode types, we performed a one-way ANOVA followed by Tukey's post-hoc test (Figure S15). The analysis, based on Coulombic efficiency data pooled across all cycles for each cell type, yielded an F value of 37.4 and a p-value of  $5.9 \times 10^{-35}$ , confirming significant differences in population means ( $p < 0.05$ ). Post-hoc analysis revealed that the 400C-Bi electrodes exhibit significantly lower Coulombic efficiency compared to all other electrode types, which did not differ significantly among themselves. These findings strongly support the hypothesis that the large, agglomerated bismuth particles observed on the 400C-Bi electrodes negatively impact CE (Figure 4a). Although bismuth is typically considered an HER inhibitor,<sup>[13a]</sup> its impact on CE in this case is detrimental, likely due to the agglomerated particle morphology. While bismuth increases VE across all cases, leading to the highest EE for 400C-Bi electrodes (Figure 4b–c), this improvement must be critically assessed, as the significant drop in CE reduces the cycling life of these cells, even if the EE remains high.

After 50 cycles, the pH of the negative electrolytes increased from its initial value of 8.5 across all cells, with values of  $10.20 \pm 0.07$ ,  $10.34 \pm 0.32$ , and  $10.46 \pm 0.07$  for NA-Bi, 150C-Bi, and 400C-Bi, respectively. This increase is attributed to parasitic HER, which raises the pH of the solution, corroborating the observation that bismuth's agglomerated form on 400C-Bi electrodes compromises the cell's Coulombic efficiency.

### Bismuth Versus Water Reduction

It is debated in the literature whether bismuth suppresses HER, decreases charge transfer resistance, or simply increases sample surface area, the latter two factors being particularly

intertwined.<sup>[13a,c,14a]</sup> Our results show that on 150C and 400C electrodes, bismuth actually reduces surface area, indicating its direct electrocatalytic activity towards CrPDTA redox, rather than merely increasing surface area. Given that flow rates, tubing, membranes, and electrolytes are identical across all experiments, the decrease in ASR and the disappearance of the 4–8 kHz feature in impedance measurements on bismuth-decorated electrodes must be attributed to reduced charge transfer resistance. This suggests bismuth's primary contribution is in facilitating electron transfer, rather than HER suppression, despite claims in the literature to the contrary.<sup>[14a,20]</sup> We therefore compare the behavior of bismuth and carbon towards HER under battery-like conditions.

Cyclic voltammetry and LSV experiments in a PDTA buffer (pH 8.5) on polished glassy carbon (GC) and metallic bismuth electrodes revealed comparable surface characteristics, with capacitances of  $25.0 \mu\text{F cm}^{-2}$  for GC and  $14.6 \mu\text{F cm}^{-2}$  for bismuth, implying similar, flat surfaces (Figure S16). However, the onset of HER, arbitrarily defined as the current density reaching  $-0.1 \text{ mA cm}^{-2}$ , occurred at  $-1.3 \text{ V}$  vs. Ag/AgCl on bismuth, compared to  $-1.6 \text{ V}$  on GC (Figure 5a), indicating that bismuth catalyzes HER at less negative potentials. This is corroborated in chronoamperometric experiments where decreasing potentials were applied in two-minute steps (Figure 5b). The onset of water reduction is clearly indicated by a steep increase in current density after  $-1.3 \text{ V}$  and  $-1.6 \text{ V}$  vs. Ag/AgCl on bismuth and GC, respectively.

To verify that decreased CE is due to HER also in full cells using bismuth decorated electrodes, slow LSV scans at  $0.05 \text{ mV s}^{-1}$  were performed with the headspace of the negative electrolyte container connected to a gas chromatographer. The cell voltage was scanned from 1.2 to 1.7 V to capture the onset potential of HER and overall hydrogen generation rate (Figure 5c). The onset of hydrogen evolution is shifted to lower cell voltages on bismuth decorated electrodes, in agreement with the ex-situ experiments, reduced CE, and increased pH in the extended cycling experiments discussed above. Notably, the gas generation rate is an order of magnitude higher in presence of bismuth and worst on 400C-Bi electrodes. This trend cannot

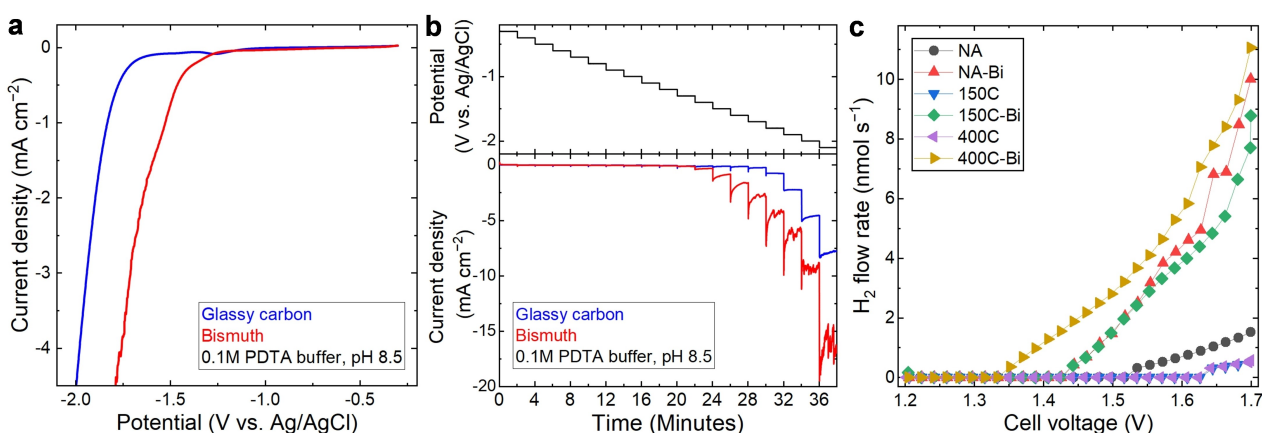


**Figure 5.** Catalytic activity of polished bismuth and glassy carbon electrodes towards hydrogen evolution. a) Linear sweep voltammetry and b) Chronoamperometry measurements on glassy carbon and metallic bismuth electrodes, c) hydrogen generation during slow linear voltage sweep in full cells for all electrode types.

be explained by differences in surface area (Table S4) and must be related to the presence of bismuth. This conclusively demonstrates that bismuth does not suppress HER as previously suggested,<sup>[13c,14a,b,21]</sup> but in fact catalyzes this parasitic side reaction.

The large, agglomerated bismuth particles found on 400C-Bi electrodes exacerbate HER, highlighting the critical role of particle morphology. Studies on CO<sub>2</sub> reduction catalysts have shown that HER can be suppressed on small, sharp dendritic particles, whereas larger, rounder aggregates promote hydrogen evolution.<sup>[22]</sup> It was proposed that sharp morphological features enhance CO<sub>2</sub> reduction by concentrating reagents via local electric fields or that sharp dendritic electrodes improve mass transport by nucleating and releasing gas bubbles at smaller sizes, especially at high current densities. Both mechanisms increase local reagent concentration through dendrite morphology, enhancing reagent reduction selectivity over hydrogen evolution.<sup>[23]</sup> Similarly, we hypothesize that optimizing bismuth deposition protocols to produce nanostructured, dendritic morphologies could favor CrPDTA reduction over HER.

## Conclusions

This study systematically investigates modifications of carbon paper electrodes and their impact on battery performance in high-voltage KCrPDTA/K<sub>4</sub>Fe(CN)<sub>6</sub> flow batteries. While thermal activation at 400°C significantly enhances wettability, surface area, and electrochemically active area, these changes do not yield the expected benefits for the chemistry studied here. The deposition of bismuth as an electrocatalyst enables power densities of up to 1.33 W cm<sup>-2</sup> by consistently lowering total cell resistance, thereby enhancing voltage and energy efficiencies. However, depending on the activation temperature, bismuth deposits exhibit a range of morphologies, with larger agglomerates significantly reducing Coulombic efficiency, posing challenges for long-term stability.

Contrary to previous reports, our findings indicate that bismuth does not necessarily increase the electrochemically active surface area but instead enhances the redox activity of the active species. Notably, we demonstrate that bismuth is a more effective catalyst for the hydrogen evolution reaction compared to bare carbon electrodes. Ultimately, this study highlights a critical trade-off between high power and longevity. While bismuth catalysts are essential for improving peak power density, addressing their impact on operational life is crucial. Developing electrode activation and electrodeposition protocols that control catalyst morphology will be key to maximizing performance in future applications.

## CRediT Statement

T.E. – investigation, formal analysis, validation, writing – original draft. F.B. – investigation, formal analysis. P.Z. – investigation, formal analysis. D. Reber – conceptualization, methodology,

investigation, formal analysis, writing – original draft, writing – review & editing, supervision, funding acquisition.

## Acknowledgements

D.R. acknowledges funding from the Swiss National Science Foundation (SNSF) Ambizione Fellowship Z00P2\_209078. D.R. also thanks Corsin Battaglia and Empa's Laboratory Materials for Energy Conversion for hosting his research group.

## Conflict of Interests

The author declares no competing interests.

## Data Availability Statement

The data that support the findings of this study are available from the corresponding author upon reasonable request.

- [1] a) Z. Li, Y.-C. Lu, *MRS Energy Sustainability* **2022**, *9*, 171–182; b) R. M. Darling, *Curr. Opin. Chem. Eng.* **2022**, *37*, 100855.
- [2] a) D. Reber, S. R. Jarvis, M. P. Marshak, *Energy Adv.* **2023**, *2*, 1357–1365; b) D. Reber, J. R. Thurston, M. Becker, M. P. Marshak, *Cell Rep. Phys. Sci.* **2023**, *4*.
- [3] K. Amini, A. N. Shocron, M. E. Suss, M. J. Aziz, *ACS Energy Lett.* **2023**, *8*, 3526–3535.
- [4] a) H. Jiang, J. Sun, L. Wei, M. Wu, W. Shyy, T. Zhao, *Energy Storage Mater.* **2020**, *24*, 529–540; b) M. Gao, Z. Wang, D. G. Lek, Q. Wang, *Nano Res. Energy* **2023**, *2*.
- [5] a) S. E. Waters, B. H. Robb, M. P. Marshak, *ACS Energy Lett.* **2020**, *5*, 1758–1762; b) S. E. Waters, B. H. Robb, S. J. Scappaticci, J. D. Saraidaridis, M. P. Marshak, *Inorg. Chem.* **2022**, *61*, 8752–8759.
- [6] D. Reber, J. R. Thurston, M. Becker, G. F. Pach, M. E. Wagoner, B. H. Robb, S. E. Waters, M. P. Marshak, *Appl. Mater. Today* **2022**, *28*, 101512.
- [7] B. H. Robb, S. E. Waters, J. D. Saraidaridis, M. P. Marshak, *Cell Rep. Phys. Sci.* **2022**, *3*.
- [8] D. Reber, *Nat. Energy* **2024**. DOI: <https://doi.org/10.1038/s41560-024-01677-6>.
- [9] R. Dmello, J. D. Milshtein, F. R. Brushett, K. C. Smith, *J. Power Sources* **2016**, *330*, 261–272.
- [10] S. E. Waters, J. R. Thurston, R. W. Armstrong, B. H. Robb, M. P. Marshak, D. Reber, *J. Power Sources* **2022**, *520*, 230877.
- [11] H. Agarwal, E. Roy, N. Singh, P. A. Klusener, R. M. Stephens, Q. T. Zhou, *Adv. Sci.* **2024**, *11*, 2307209.
- [12] a) A. M. Pezeshki, J. T. Clement, G. M. Veith, T. A. Zawodzinski, M. M. Mench, *J. Power Sources* **2015**, *294*, 333–338; b) J. Piwek, G. Gonzalez, P. Peljo, E. Frackowiak, *Carbon* **2023**, *215*, 118483; c) K. Köble, M. Jaugstetter, M. Schilling, M. Braig, T. Diemant, K. Tschulik, R. Zeis, *J. Power Sources* **2023**, *569*, 233010; d) K. V. Greco, A. Forner-Cuenca, A. Mularczyk, J. Eller, F. R. Brushett, *ACS Appl. Mater. Interfaces* **2018**, *10*, 44430–44442.
- [13] a) M. Wu, M. Fang, M. Nan, X. Chen, X. Ma, *Chem. Asian J.* **2023**, *18*, e202201242; b) D. J. Suárez, Z. González, C. Blanco, M. Granda, R. Menéndez, R. Santamaría, *ChemSusChem* **2014**, *7*, 914–918; c) K. Amini, J. Gostick, M. D. Pritzker, *Adv. Funct. Mater.* **2020**, *30*, 1910564.
- [14] a) Y. Ahn, J. Moon, S. E. Park, J. Shin, J. W. Choi, K. J. Kim, *Chem. Eng. J.* **2021**, *421*, 127855; b) G. Wei, X. Fan, J. Liu, C. Yan, *J. Power Sources* **2015**, *281*, 1–6; c) T. Liu, X. Li, H. Nie, C. Xu, H. Zhang, *J. Power Sources* **2015**, *286*, 73–81.
- [15] R. Schweiss, C. Meiser, T. Damjanovic, I. Galbiati, N. Haak, *White paper SGL Group* **2016**, 267.
- [16] F. Tuinstra, J. L. Koenig, *J. Chem. Phys.* **1970**, *53*, 1126–1130.
- [17] A. C. Ferrari, J. Robertson, *Phys. Rev. B* **2000**, *61*, 14095.

- [18] M. Cecchetti, M. Messaggi, A. Donazzi, A. Facibeni, V. Russo, C. Casari, A. L. Bassi, A. Casalegno, M. Zago, *Electrochim. Acta* **2020**, *329*, 135143.
- [19] R.-S. Kühnel, D. Reber, C. Battaglia, *J. Electrochem. Soc.* **2020**, *167*, 070544.
- [20] a) H. Zhang, Y. Tan, J. Li, B. Xue, *Electrochim. Acta* **2017**, *248*, 603–613; b) S. R. Tirukkovalluri, R. K. H. Gorthi, *J. New Mater. Electrochem. Syst.* **2013**, *16*, 287–292.
- [21] Y. Liu, F. Liang, Y. Zhao, L. Yu, L. Liu, J. Xi, *J. Energy Chem.* **2018**, *27*, 1333–1340.
- [22] W. Ju, J. Zeng, K. Bejtka, H. Ma, D. Rentsch, M. Castellino, A. Sacco, C. F. Pirri, C. Battaglia, *ACS Appl. Energ. Mater.* **2018**, *2*, 867–872.
- [23] a) M. Liu, Y. Pang, B. Zhang, P. De Luna, O. Voznyy, J. Xu, X. Zheng, C. T. Dinh, F. Fan, C. Cao, *Nature* **2016**, *537*, 382–386; b) T. Burdyny, P. J. Graham, Y. Pang, C.-T. Dinh, M. Liu, E. H. Sargent, D. Sinton, *ACS Sustainable Chem. Eng.* **2017**, *5*, 4031–4040.

---

Manuscript received: October 31, 2024  
Revised manuscript received: November 28, 2024  
Accepted manuscript online: November 28, 2024  
Version of record online: December 6, 2024